Electronic Supplementary Material (ESI) for Catalysis Science & Technology.

Supporting Information

Environment-Benign General Synthesis of Inconsecutive Carbon Coated RuP_2 Porous Microsheet as Efficient Bifunctional Electrocatalysts in Neutral Condition Enables Energy-Saving H_2 Production under Hybrid Water Electrolysis

Yapeng Li,[#] Wentao Wang, [#] Mingyu Cheng, [#] Qizhu Qian, Yin Zhu and Genqiang Zhang[*1]

Dr. Y. P. Li, Mr. M. Y. Cheng, Mr. Q. Z. Qian, Ms. Y. Zhu and Prof. G. Q. Zhang
Hefei National Laboratory for Physical Sciences at the Microscale, CAS Key Laboratory of Materials for Energy Conversion, Department of Materials Science and Engineering, University of Science and Technology of China, Hefei, Anhui 230026, China
Email: gqzhangmse@ustc.edu.cn

Prof. W. T. Wang
Guizhou Provincial Key Laboratory of Computational Nano-Material Science, Guizhou Education University, Guiyang 550018, China

+ These authors contribute equally to this work.

1. Experimental section

1.1. *Synthesis of RuP_2@InC-MS*

The equal GP and melamine (1.5 mmol, respectively) were uniformly dispersed in 15 ml ethanol, and then 0.1 mmol $RuCl_3$ was added in the above mixture and stirred for 15 min. Then, the mixture was centrifuged to obtain the yellowish product. Finally, the black product of RuP_2@InC-MS can be easily synthesized via a one-pot pyrolysis at 850 ^{o}C for 2 h with a heating rate of 2 ^{o}C min^{-1} under Ar atmosphere. Just changing the P source to AP or AuP can obtain the other two kinds of RuP_2@InC-MS.

1.2. *Synthesis of RuP_2 MS*

The method is similar with the above RuP_2@InC-MS except for no adding melamine.

1.3. *Synthesis of the other transition metal phosphides*

The other transition metal phosphides including PtP_2, Pd_5P_2, Ni_2P, CoP, and FeP are synthesized via the similar method except substituting the $RuCl_3$ with $PtCl_4$, $PdCl_2$, $Ni(Ac)_2$, $Co(Ac)_2$, $FeCl_3$, respectively.

1.4. *Materials characterization*

The morphology was observed via the field-emission scanning electron microscopy (FESEM, SU-8200); the microstructure and elemental distribution was characterized by transmission electron microscopy (TEM, JEOL, JEM-2010) equipped with energy disperse spectroscopy (EDS); powder X-ray diffractor (XRD, TTR-III) was used to explore the phase; X-ray photoelectron spectroscopy (XPS, ESCALAB 250) was executed to analyze the elemental information; gas chromatographs (GC 7900) equipped with a thermal conductivity detector and TDX-01 column was utilized to analyze the generated H_2.

1.5. *Computational details*.

Density functional theory (DFT) based first-principles calculations are performed using the projected augmented wave (PAW)[1] method implemented in the Vienna *ab initio* simulation package (VASP). The Kohn-Sham one-electron states are expanded using the plane wave basis set with a kinetic energy cutoff of 550 eV. The Perdew-Burke-Ernzerhof (PBE)[2] exchange-correlation functional within the generalized gradient approximation (GGA) is employed. The Ru-terminated (3 × 1) RuP_2 (110) surface slab of 11 layers is a rectangular cell of 8.567 Å ×7.592 Å, which can nicely match with 2√3×3 unit cell of graphene (8.521 Å × 7.380 Å). For the heterostructures studied in this work, we used the averaged lateral lattice constants (of the supercells) to minimize the strains on both subsystems. The active surface is Ru-terminated (3 × 1) RuP_2 (110) surface. The P atom substitutes one of the graphene C to model the P: graphene/RuP_2. The Brillouin-zone (BZ) integration is carried out using the Monkhorst-Pack sampling method with a density of 4×4×1 for the geometry optimizations. A vacuum layer of 15 Å is included to avoid the interaction between neighboring slabs. All atoms are fully relaxed until the maximum magnitude of the force acting on the atoms is smaller than 0.03 eV/Å.

In order to evaluate the stability of the relaxed model, the surface energy of RuP_2 and the interface adhesion energy of RuP_2@InC-MS have been calculated.

The surface energy of RuP_2 can be written as[3]:

$$\gamma_{RuP_2} = [E^{slab}(RuP_2) - N_P/2 \times E^{bulk}(RuP_2) - (N_{Ru} - N_P/2) \times E^{bulk}(Ru)]/2A \quad (1)$$

where $E^{slab}(RuP_2)$ is the energy of the RuP_2 surface slab; $E^{bulk}(RuP_2)$ is the energy per formula unit of the bulk RuP_2; $E^{bulk}(Ru)$ is the energy per formula unit of the bulk Ru; N_P and N_{Ru} are the numbers of P and Ru atoms in the surface slab, and the A is the cross-sectional area of the surface slab. The surface energy of RuP_2 is calculated to be 2.52 J m^{-2}, much lower than those of reported transition metal compound[4], suggesting that the (3 × 1) RuP_2 (110) with the Ru-termination surface is more energetically favorable.

The interface adhesion energy of RuP_2@InC-MS is used to judge the stability of the system and was defined as[5]:

$$E(ad) = E(RuP_2@InC\text{-}MS) - E[RuP_2] - E[InC\text{-}MS] \quad (2)$$

where $E(RuP_2$@InC-MS), $E[RuP_2]$, and E [InC-MS] represent the total energies of the relaxed RuP_2@InC-MS, pure RuP_2, and pure InC-MS, respectively. If the value of the adhesion energy is negative, the interface is stable. The adhesion energy of the RuP_2@InC-MS is calculated to be -0.05 eV $Å^{-2}$, which indicates that this interface was stable.

Under the standard condition, the overall HER pathway includes two steps: first, adsorption of hydrogen on the catalytic site (*) from the initial state ($H^+ + e^- + *$), second, releasing the product hydrogen (1/2 H_2). The total energies of $H^+ + e^-$ and ½ H_2 are equal. Therefore, the Gibbs free energy of the adsorption of the intermediate hydrogen on a catalyst (ΔG_H) is the key descriptor of the HER activity of the catalyst and is obtained by:

$$\Delta G_H = \Delta E_H + \Delta ZPE - T\Delta S$$

where ΔE_H, ΔZPE, and ΔS are the adsorption energy, zero-point energy change and entropy change of H adsorption, respectively.

The oxidation of hydrazine into nitrogen and hydrogen occurs in the following six consecutive elementary steps:

(A) $* + N_2H_4 \rightarrow *N_2H_4$, (3)

(B) $*N_2H_4 \rightarrow *N_2H_3 + H^+ + e-$, (4)

(C) $*N_2H_3 \rightarrow *N_2H_2 + H^+ + e-$, (5)

(D) $*N_2H_2 \rightarrow *N_2H + H^+ + e-$, (6)

(E) $*N_2H \rightarrow *N_2 + H^+ + e-$, (7)

(F) $*N_2 \rightarrow * + N_2$. (8)

The asterisk (*) represents the reaction surface of these calculated RuP_2 (110), and RuP_2-C MS (110). "$*N_2H_4$", "N_2H_3", "N_2H_2", "N_2H", and "$*N_2$" denote the models with the corresponding chemisorbed species residing in the reaction surfaces. Among these six elementary steps, steps (A) and (F) are the adsorption of N_2H_4 and desorption of N_2, respectively. The other four elementary steps involve the generation of one proton and one electron. Then, using the computational hydrogen electrode (pH = 0, p = 1 atm, T = 298 K), the Gibbs free energy of $H^+ + e^-$ is replaced implicitly with the Gibbs free energy of one-half a H_2 molecule. Thus the reaction Gibbs free energies can be calculated with eqs[6]:

$$\triangle G_A = \triangle G_{*N_2H_4} - \triangle G_{*} - \triangle G_{N_2H_4} \quad (9)$$

$$\triangle G_B = \triangle G_{*N_2H_3} + 0.5\triangle G_{H_2} - \triangle G_{*N_2H_4} - eU - kT\ln 10{*}pH \quad (10)$$

$$\triangle G_C = \triangle G_{*N_2H_2} + 0.5\triangle G_{H_2} - \triangle G_{*N_2H_3} - eU - kT\ln 10{*}pH \quad (11)$$

$$\triangle G_D = \triangle G_{*N_2H} + 0.5\triangle G_{H_2} - \triangle G_{*N_2H_2} - eU - kT\ln 10{*}pH \quad (12)$$

$$\triangle G_E = \triangle G_{*N_2} + 0.5\triangle G_{H_2} - \triangle G_{*N_2H} - eU - kT\ln 10{*}pH \quad (13)$$

$$\triangle G_F = \triangle G_{*} + G_{N_2} - \triangle G_{*N_2} \quad (14)$$

U and the pH value in this work is set to zero. The adsorption or reaction Gibbs free energy is defined as: $\Delta G = \Delta E + (ZPE - T\Delta S)$, where ΔE is the adsorption or reaction energy based on DFT calculations, ΔZPE is the zero point energy (ZPE) correction, T is the temperature, and ΔS is the entropy change. For each system, its ZPE can be calculated by summing vibrational frequencies over all normal modes v ($ZPE = 1/2\Sigma\hbar v$). The entropies of gas phase H_2, N_2, and NH_2NH_2 are obtained from the NIST database[7] with the standard condition, and the adsorbed species are only taken vibrational entropy (Sv) into account, as shown in the following formula:

$$Sv=\sum_i R\{hv_i/[k_BT{*}\exp(hv_i/k_BT)-k_BT]-\ln[1-\exp(-hv_i/k_BT)]\} \quad (15)$$

Among which R = 8.314 $J\cdot mol^{-1}\cdot K^{-1}$, T = 298.15 K, h = 6.63 $\times 10^{-34}$ J·s, $k_B = 1.38 \times 10^{-23}$ $J\cdot K^{-1}$, i is the frequency number, v_i is the vibrational frequency (unit is cm^{-1}).

The charge transfer between N_2H_4 dehydrogenation intermediate (“$*N_2H_4$”, “$*N_2H_3$”, “$*N_2H_2$”, “$*N_2H$”, and “$*N_2$”) adsorbing material surface was estimated by employing the Bader Charge Analysis version 1.03.[8, 9]

The charge density difference ($\Delta\rho$) was obtained using the following equation: $\Delta\rho = \rho(\text{surface} + \text{intermediate}) - \rho(\text{surface}) - \rho(\text{intermediate})$, where $\rho(\text{surface} + \text{intermediate})$, $\rho(\text{surface})$ and $\rho(\text{intermediate})$ are the total charge density of the N_2H_4 dehydrogenation intermediate (“$*N_2H_4$”, “$*N_2H_3$”,“$*N_2H_2$”, “$*N_2H$”, and “$*N_2$”) adsorbed RuP_2 (110) (RuP2 and RuP_2-C MS) surface, and N_2H_4 dehydrogenation intermediate (“$*N_2H_4$”, “$*N_2H_3$”,“$*N_2H_2$”, “$*N_2H$”, and “$*N_2$”), respectively. The charge density difference quantifies the redistribution of electron charge due to the interaction between N_2H_4 dehydrogenation intermediate (“$*N_2H_4$”, “$*N_2H_3$”, “$*N_2H_2$”, “$*N_2H$”, and “$*N_2$”) and RuP_2 (110) surface of both the two samples.

2. Characterization

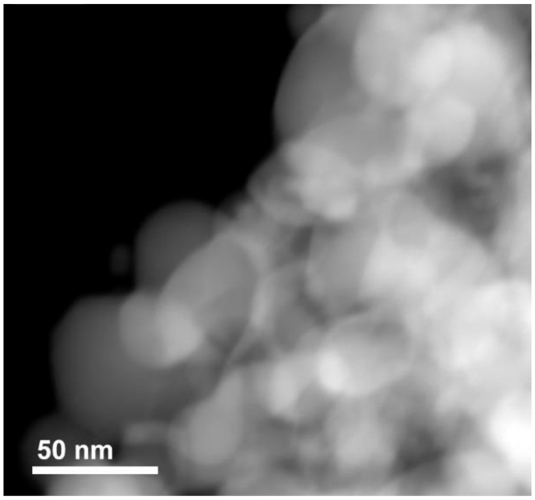

Figure S1. The HAADF-STEM image of RuP_2@InC-MS.

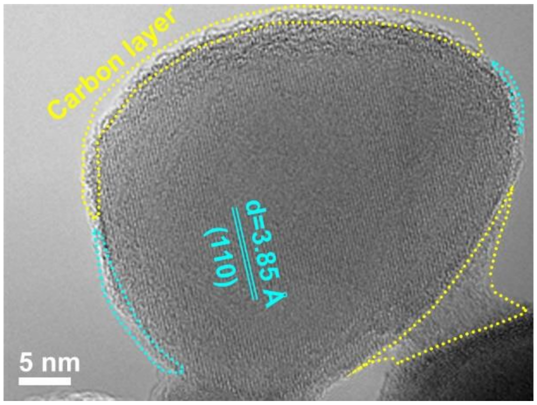

Figure S2. The HRTEM image of a single particle in RuP_2@InC-MS.

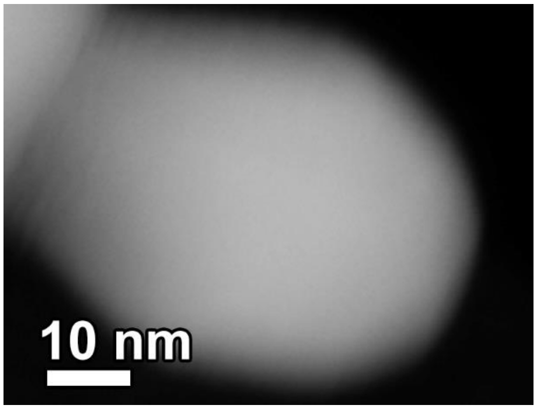

Figure S3. The HAADF-STEM image of a single particle in RuP_2@InC-MS.

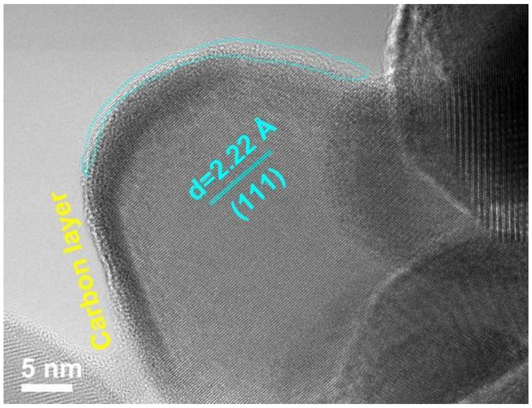

Figure S4. The microstructure characterization of RuP_2@InC-MS.

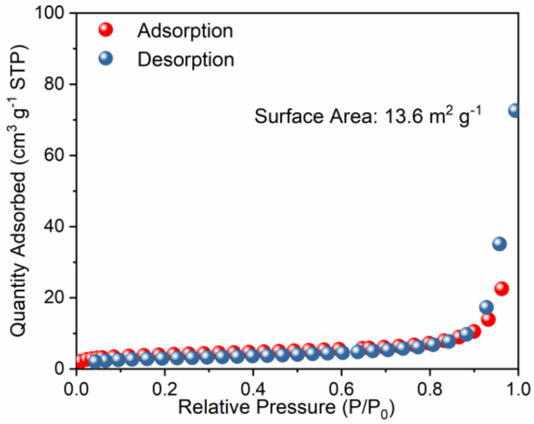

Figure S5. The Nitrogen Adsorption-desorption isotherm carve of RuP_2@InC-MS.

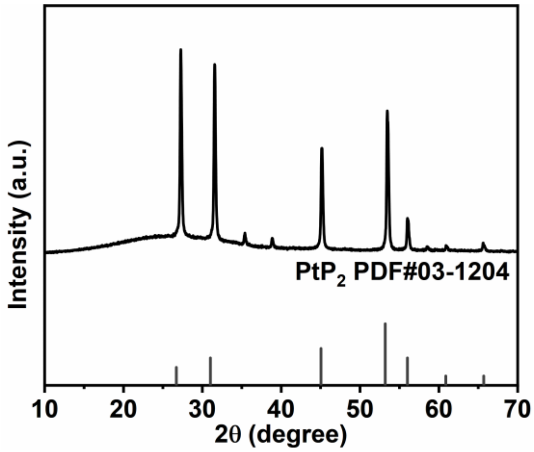

Figure S6. The XRD pattern of PtP_2.

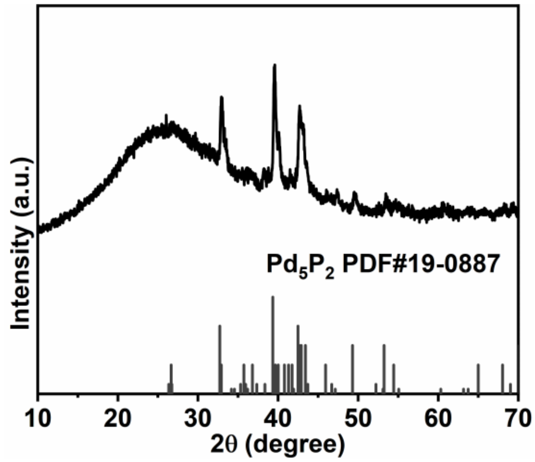

Figure S7. The XRD pattern of Rd_5P_2.

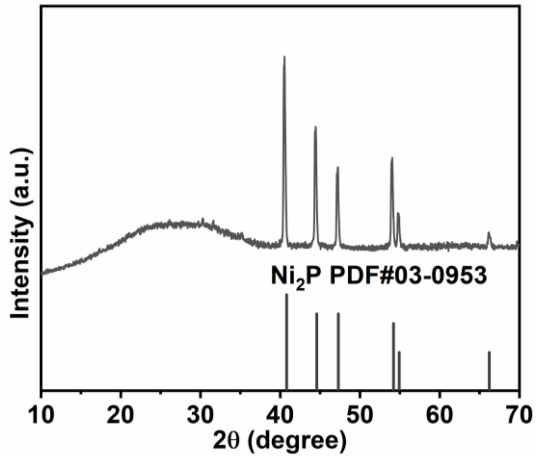

Figure S8. The XRD pattern of Ni_2P.

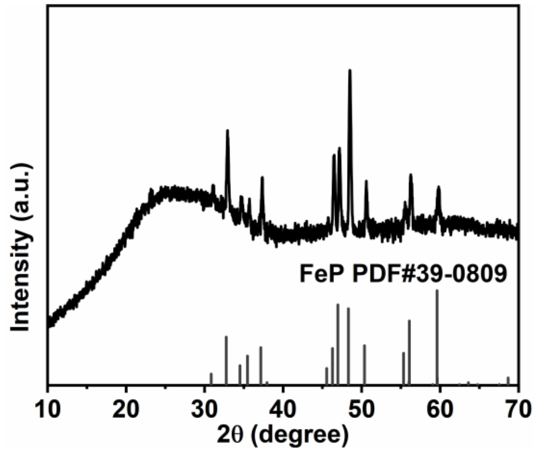

Figure S9. The XRD pattern of FeP.

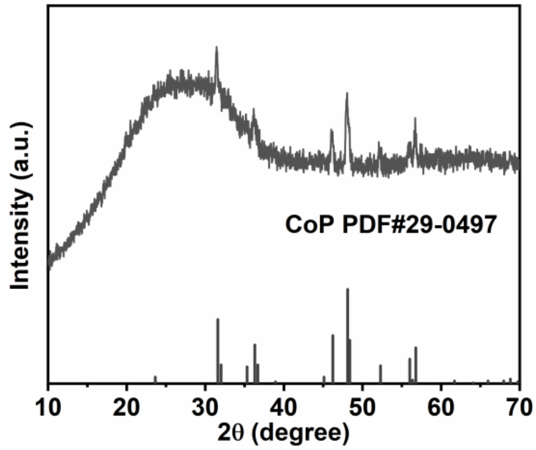

Figure S10. The XRD pattern of CoP.

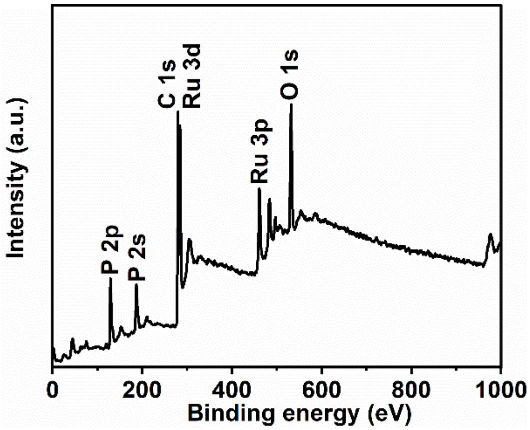

Figure S11. The XPS survey spectrum of RuP_2@InC-MS.

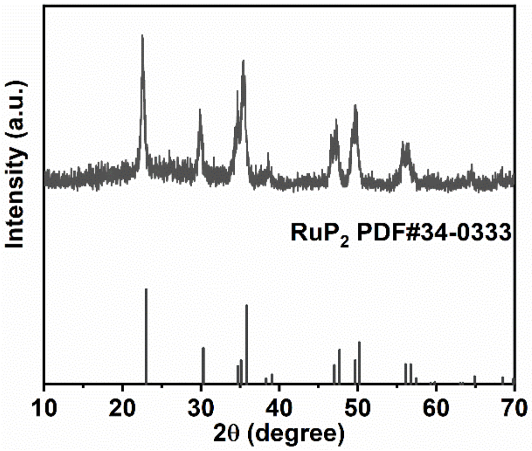

Figure S12. The XRD pattern of the RuP_2@InC-MS synthesized with AuP as P source.

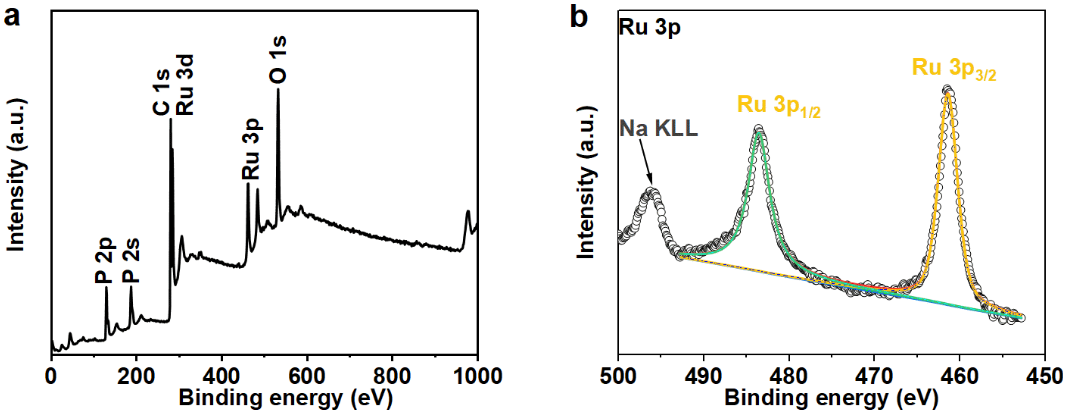

Figure S13. The survey (a) and Ru 3p spectra (b) of RuP_2@InC-MS synthesized with AuP as P source.

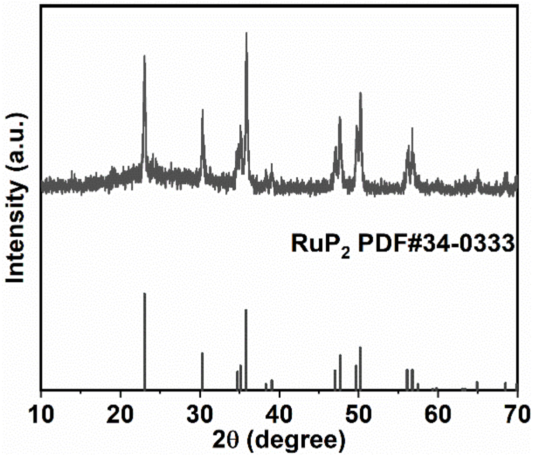

Figure S14. The XRD pattern of the RuP_2@InC-MS synthesized with AP as P source.

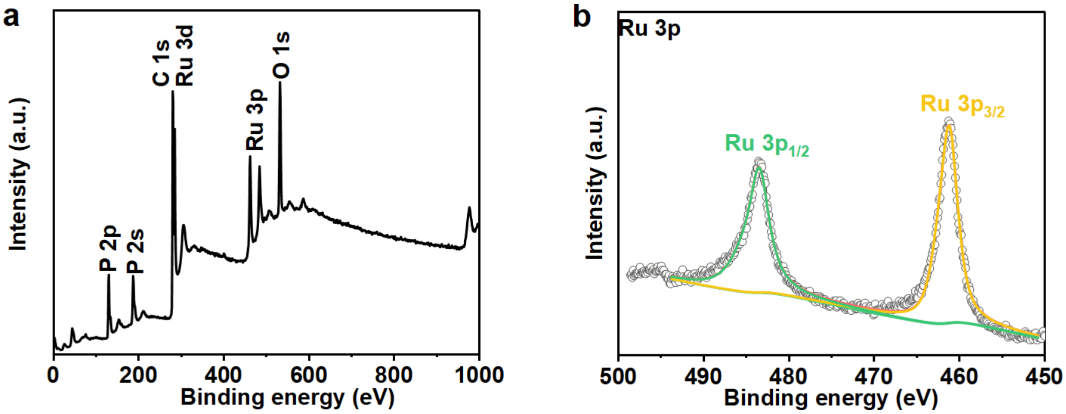

Figure S15. The survey (a) and Ru 3p spectra (b) of RuP_2@InC-MS synthesized with AP as P source.

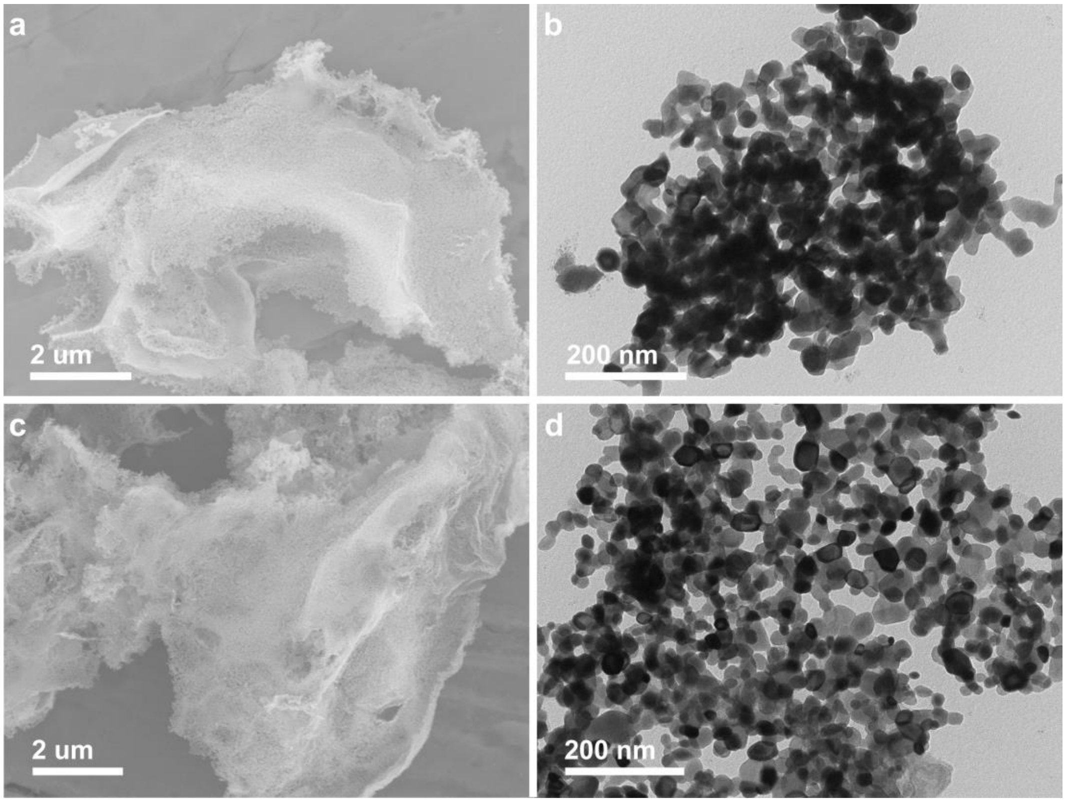

Figure S16. The morphology characterization of the RuP_2@InC-MS synthesized with different amounts of GP: (a, b) 5 mmol. (c, d) 30 mmol.

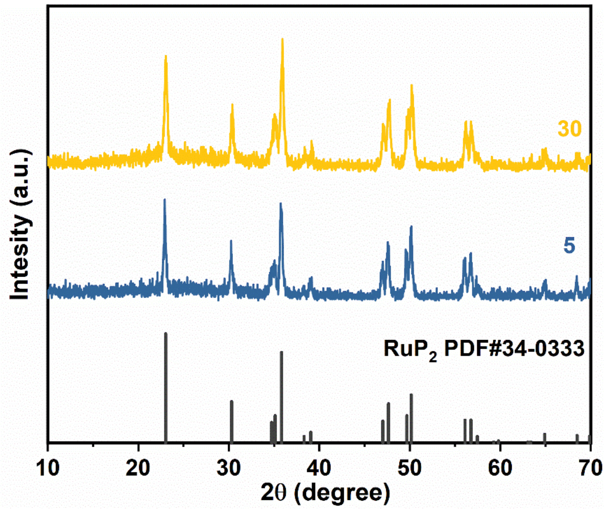

Figure S17. The XRD patterns of RuP_2@InC-MS synthesized at 850 °C with different content of GP (5 mmol, 30 mmol).

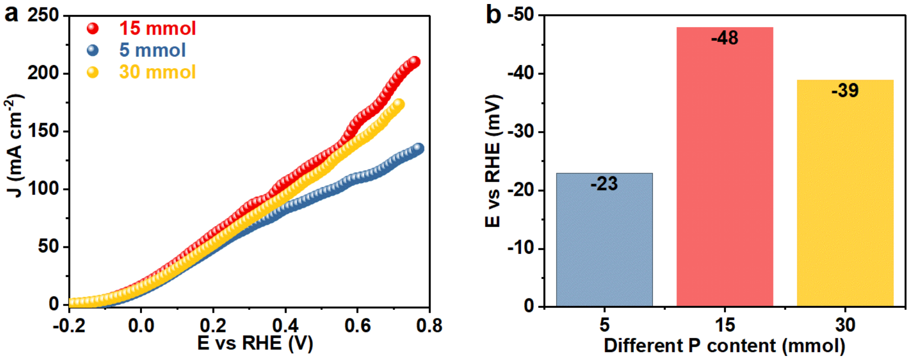

Figure S18. The HzOR performance optimization of RuP_2@InC-MS synthesized with different amounts of GP (5, 15, 30 mmol): (a) The LSV curves in 1.0 M PBS + 1.0 M N_2H_4 with scan rate of 5 mV s^{-1}. (b) The comparing working potentials at 10 mA cm^{-2}.

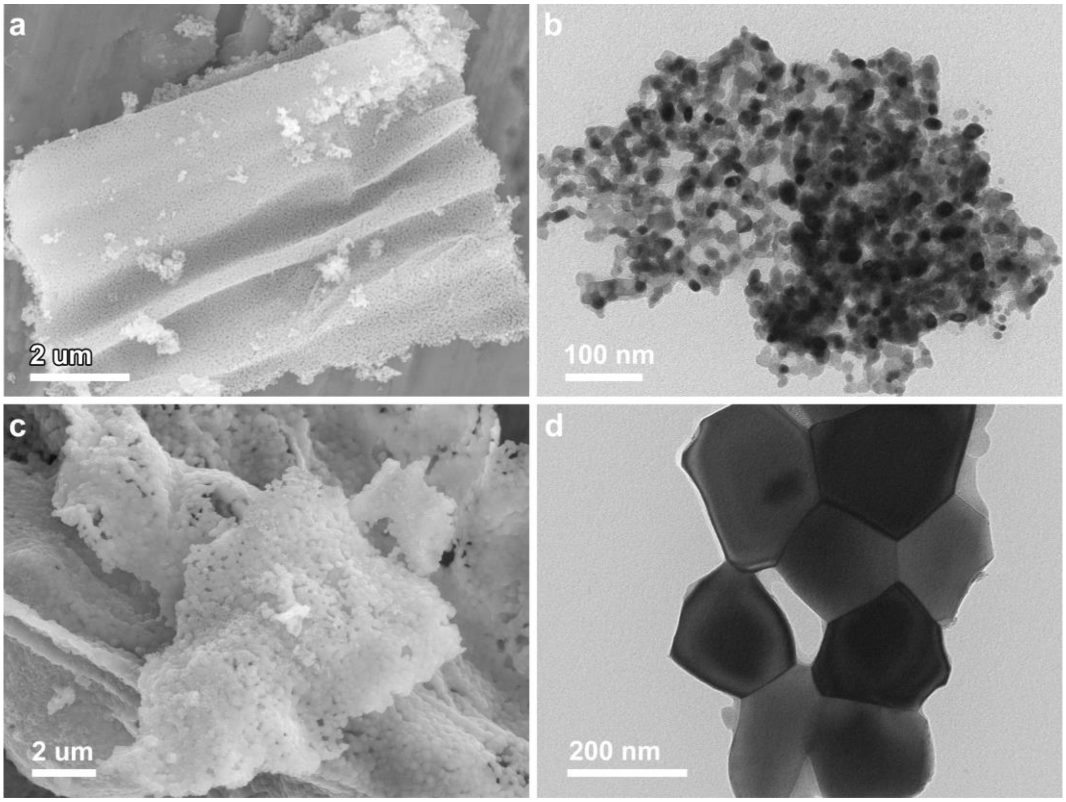

Figure S19. The morphology characterization of the RuP_2@InC-MS synthesized with 15 mmol of GP at different temperatures: (a, b) 800 °C. (c, d) 900 °C.

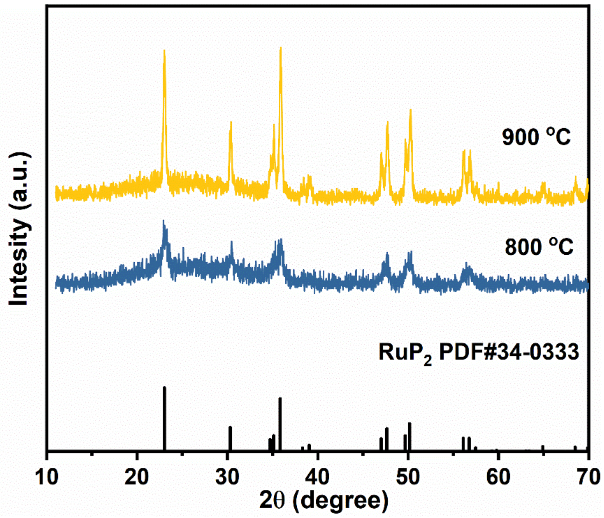

Figure S20. The XRD patterns of RuP_2@InC-MS synthesized at different temperatures (800 °C, 900 °C) with 15 mmol of GP.

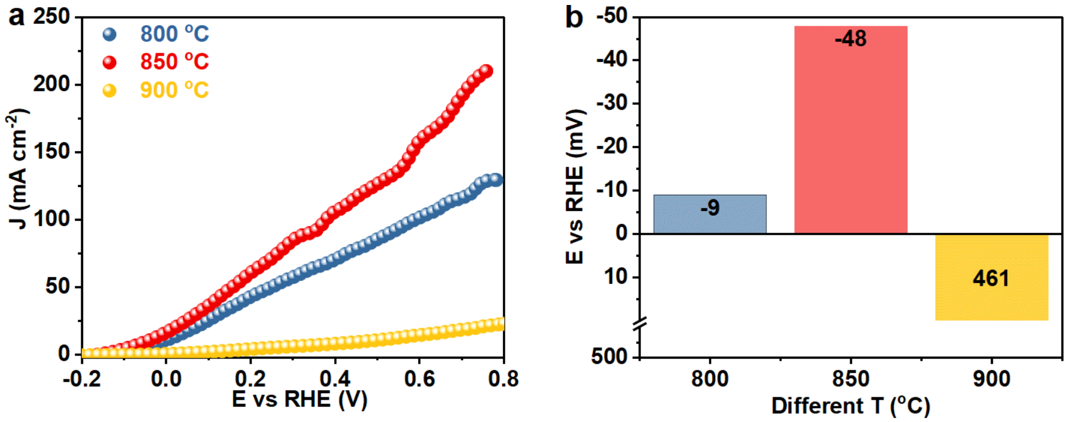

Figure S21. The HzOR performance optimization of RuP$_2$@InC-MS synthesized under different temperatures (800, 850, 900 °C) with 15 mmol of GP: (a) The LSV curves in 1.0 M PBS + 1.0 M N_2H_4 with scan rate of 5 mV s^{-1}. (b) The comparing working potentials at 10 mA cm^{-2}.

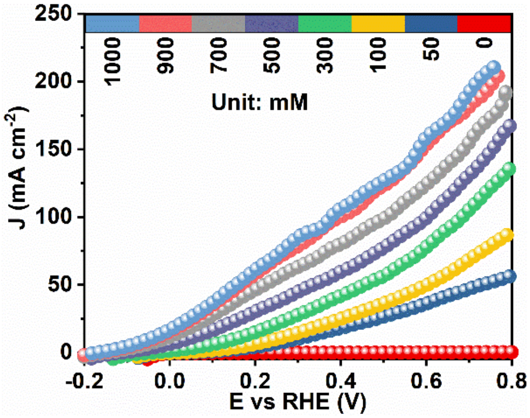

Figure S22. The LSV curves of RuP$_2$@InC-MS in 1.0 M PBS containing variable concentrations of hydrazine.

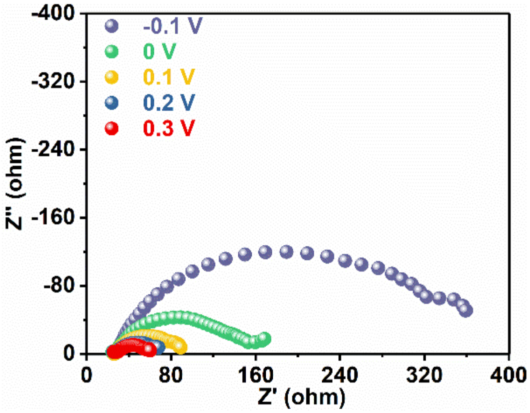

Figure S23. The Nyquist plots of RuP$_2$@InC-MS in 1.0 M PBS + 1.0 M N_2H_4 at different potentials.

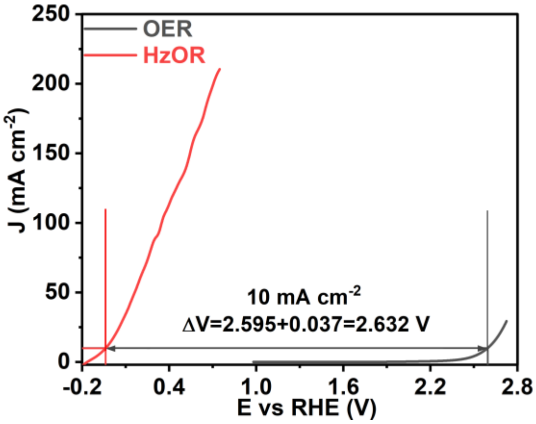

Figure S24. The comparing LSV curves toward OER and HzOR.

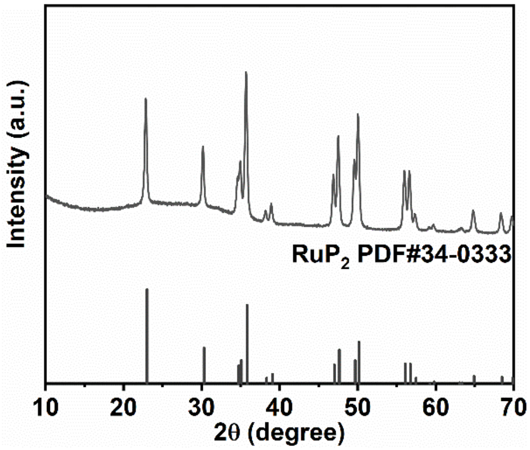

Figure S25. The XRD pattern of RuP_2 synthesized via the thermal treatment of the mixture of $RuCl_3$ and the red P.

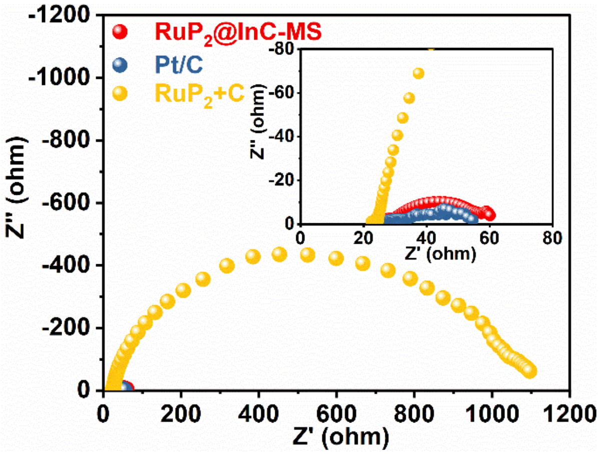

Figure S26. The Nyquist plots of RuP_2@InC-MS, Pt/C, and RuP_2+C at 0.3 V vs RHE in 1.0 M PBS + 1.0 M N_2H_4.

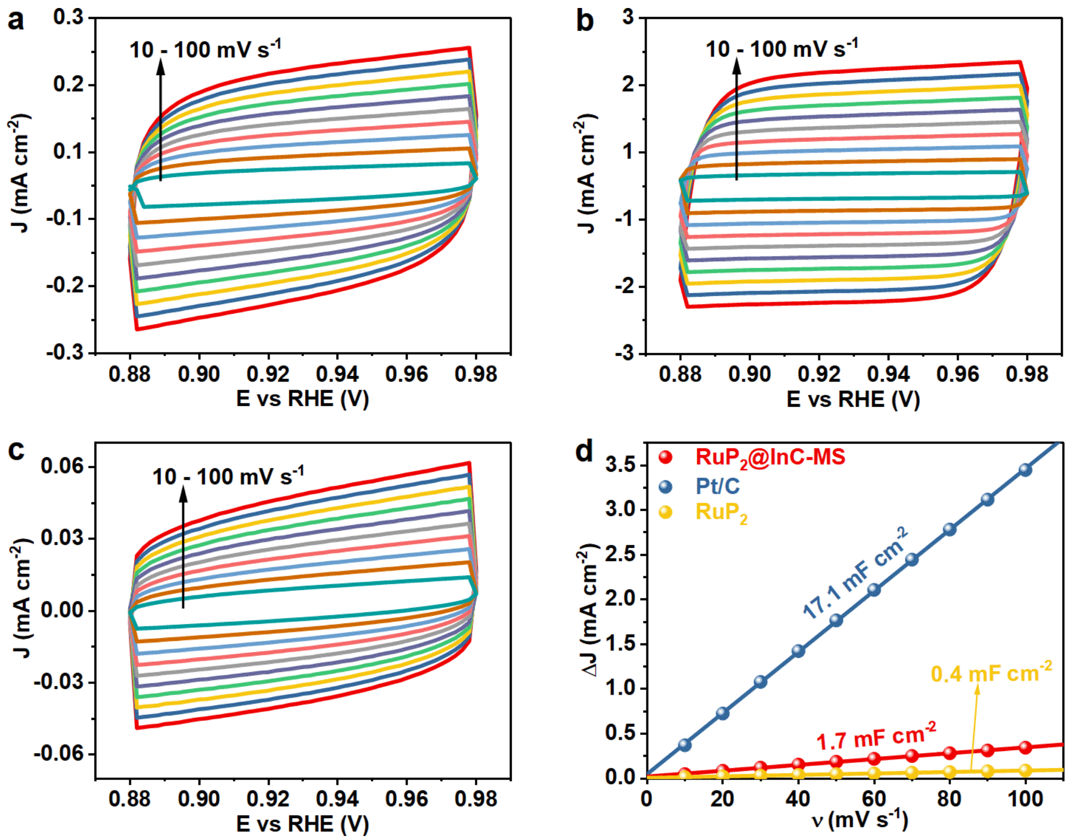

Figure S27. The ECSAs investigation of RuP_2@InC-MS, Pt/C, and RuP_2. The CV curves of RuP_2@InC-MS (a), Pt/C (b), and RuP_2 (c) with the scan rate of 10-100 mV s^{-1}. (d) The linear relationships of the current density gaps with the scan rate and the responding C_{dl} values at 0.94 V vs RHE.

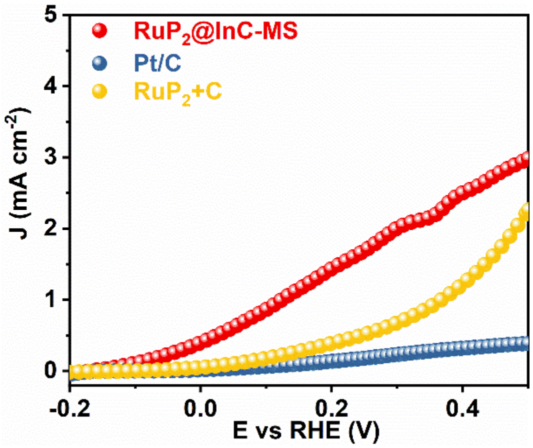

Figure S28. The ECSA corrected HzOR LSV curves.

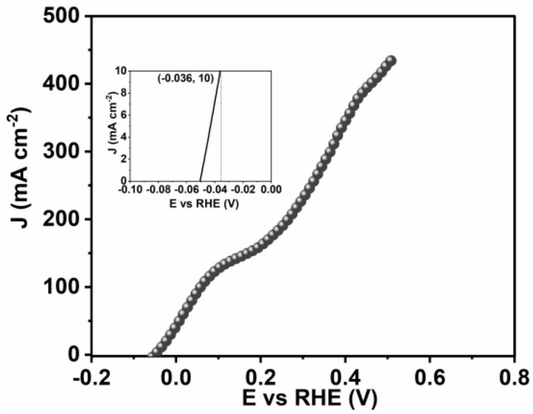

Figure S29. The HzOR performance of RuP_2@InC-MS in 1.0 M KOH + 0.3 M N_2H_4.

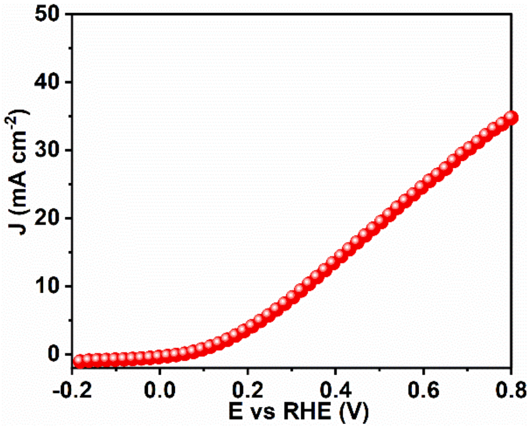

Figure S30. The HzOR LSV curve of RuP_2@InC-MS in simulated wastewater contained 1.0 M N_2H_4. The per liter wastewater contains: 1.64 g NaAc, 0.47 g NH_4Cl, 1.0 g NaCl, 3 g KH_2PO_4, 17.8 g Na_2HPO_4•$12H_2O$, 0.011 g $CaCl_2$, and 0.12 g $MgSO_4$.

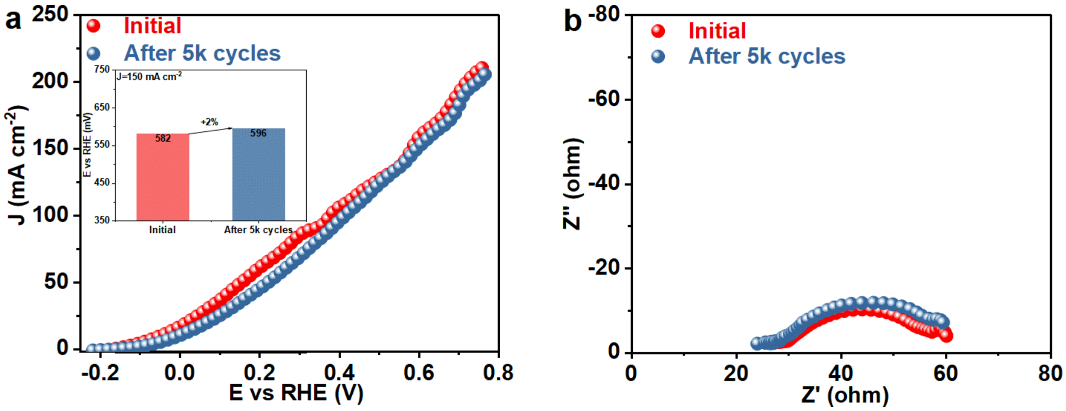

Figure S31. The stability investigation of RuP_2@InC-MS for HzOR in 1.0 M KOH + 1.0 M N_2H_4: (a) The initial and after 5k cycle's LSV curves, inset shows the comparing working potential at 150 mA cm^{-2}. (b) The comparing Nyquist plots.

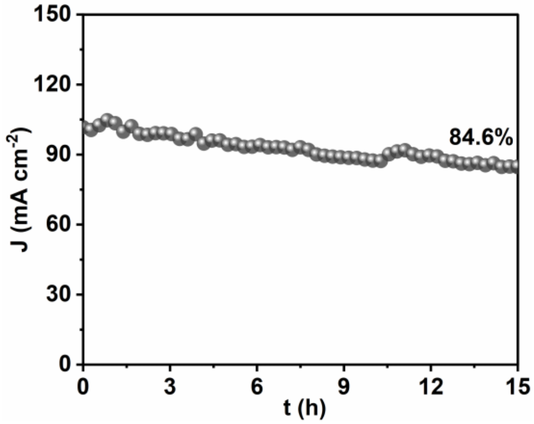

Figure S32. The i-t curves of the HzOR proves at the working potential of 530 mV without iR correction.

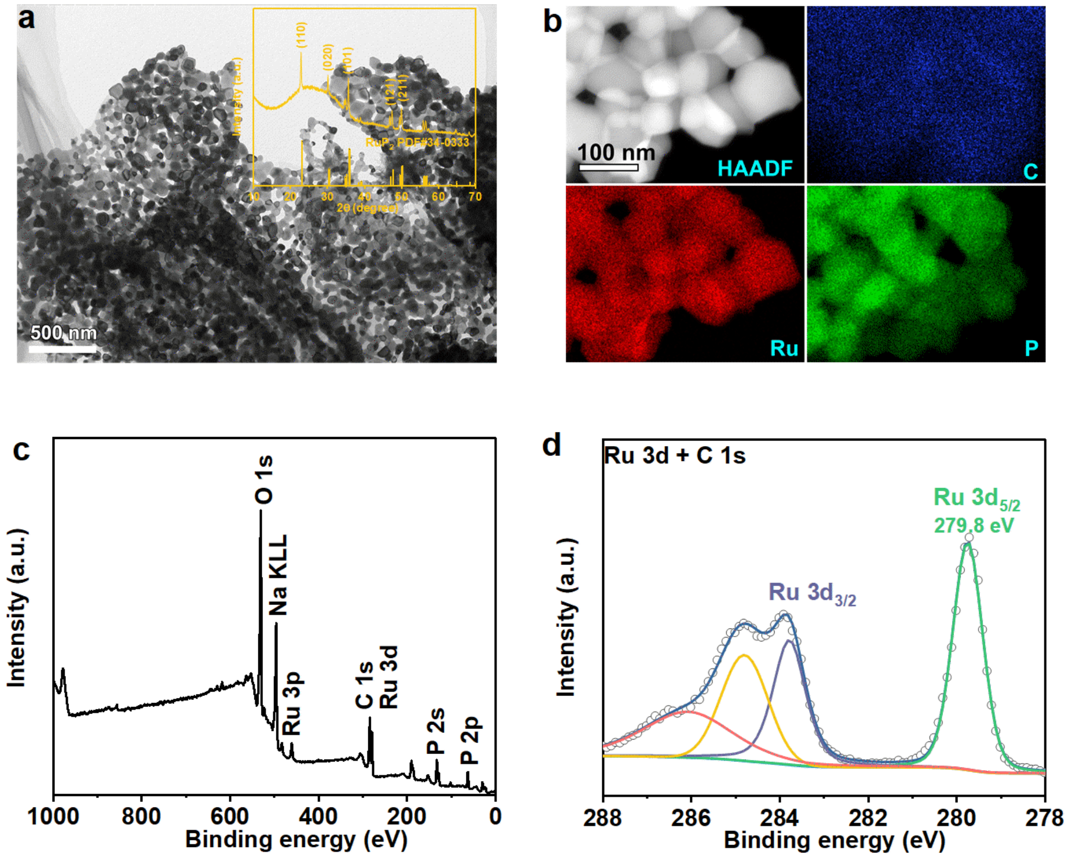

Figure S33. The morphology and structure characterization of RuP$_2$@InC-MS after HzOR stability test in 1.0 M KOH + 1.0 M N_2H_4: (a) The TEM image, inset shows the XRD pattern. (b) The HAADF-STEM and the corresponding EDS mapping. (c) The survey spectrum and (d) Ru 3d + C 1s high-resolution spectrum.

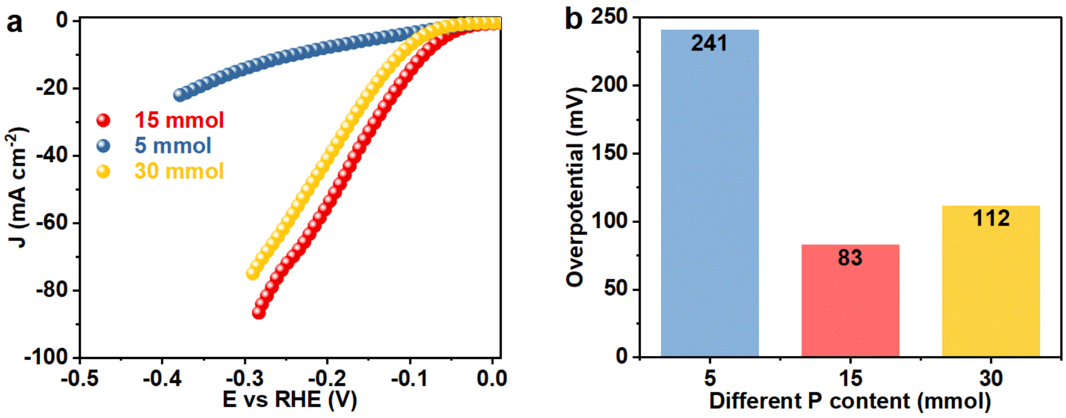

Figure S34. The P content optimization of RuP$_2$@InC-MS: (a) The LSV curves in 1.0 M PBS with scan rate of 5 mV s^{-1}. (b) The comparing working potential at 10 mA cm^{-2}.

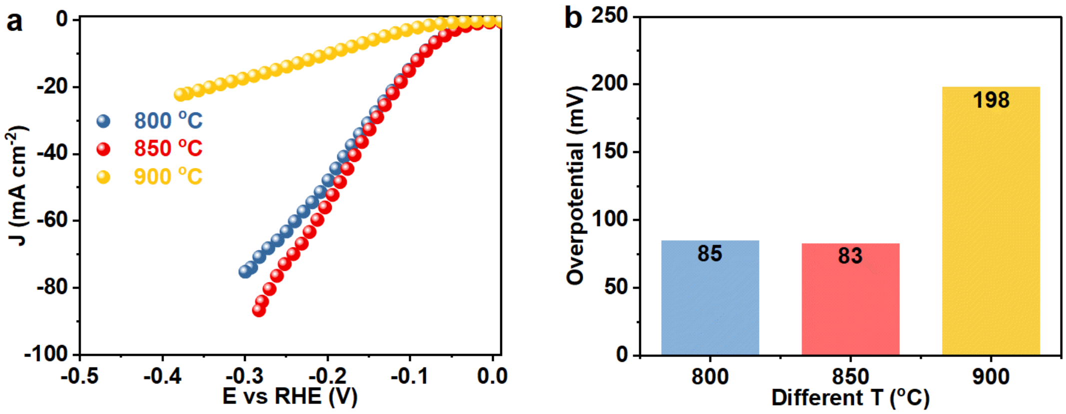

Figure S35. The annealing temperature optimization of RuP$_2$@InC-MS toward HER: (a) The LSV curves in 1.0 M PBS with scan rate of 5 mV s^{-1}. (b) The comparing working potential at 10 mA cm^{-2}.

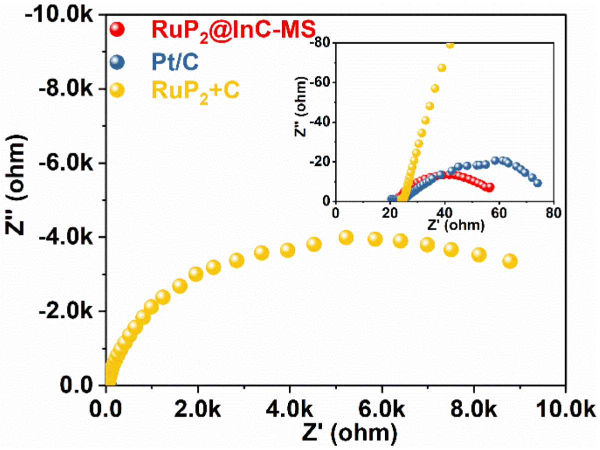

Figure S36. The Nyquist plots of RuP2@InC-MS, Pt/C, and RuP2+C at the overpotential of 100 mV in 1.0 M PBS.

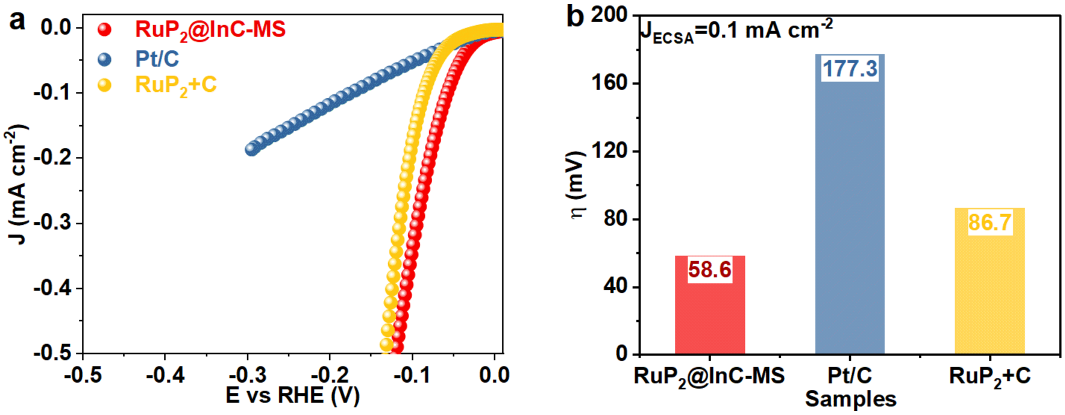

Figure S37. The specific HER performance of RuP2@InC-MS, Pt/C, and RuP2+C: (a) ECSA normalized polarization curves. (b) The comparing overpotentials at the specific current density of 0.1 mV cm^{-2}.

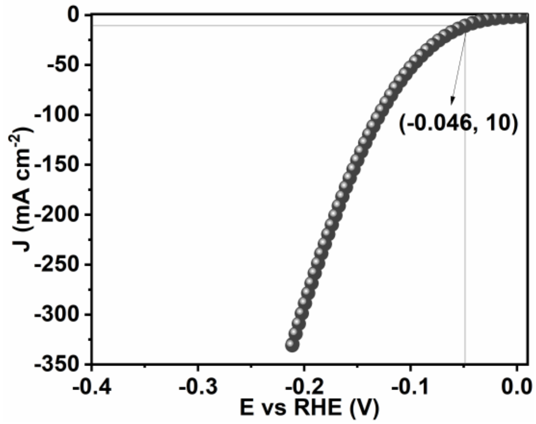

Figure S38. The HER polarization curve of RuP_2@InC-MS in 1.0 M KOH.

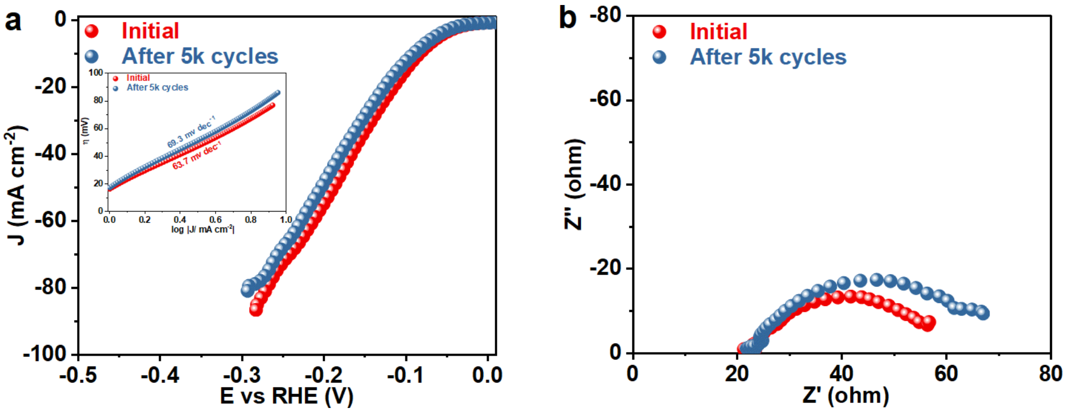

Figure S39. The electrochemical performance after ADT test: The initial and 5k cycles' LSV curves (a) and Nyquist plots at the overpotential of 100 mV (b), inset is the corresponding Tafel slope plots.

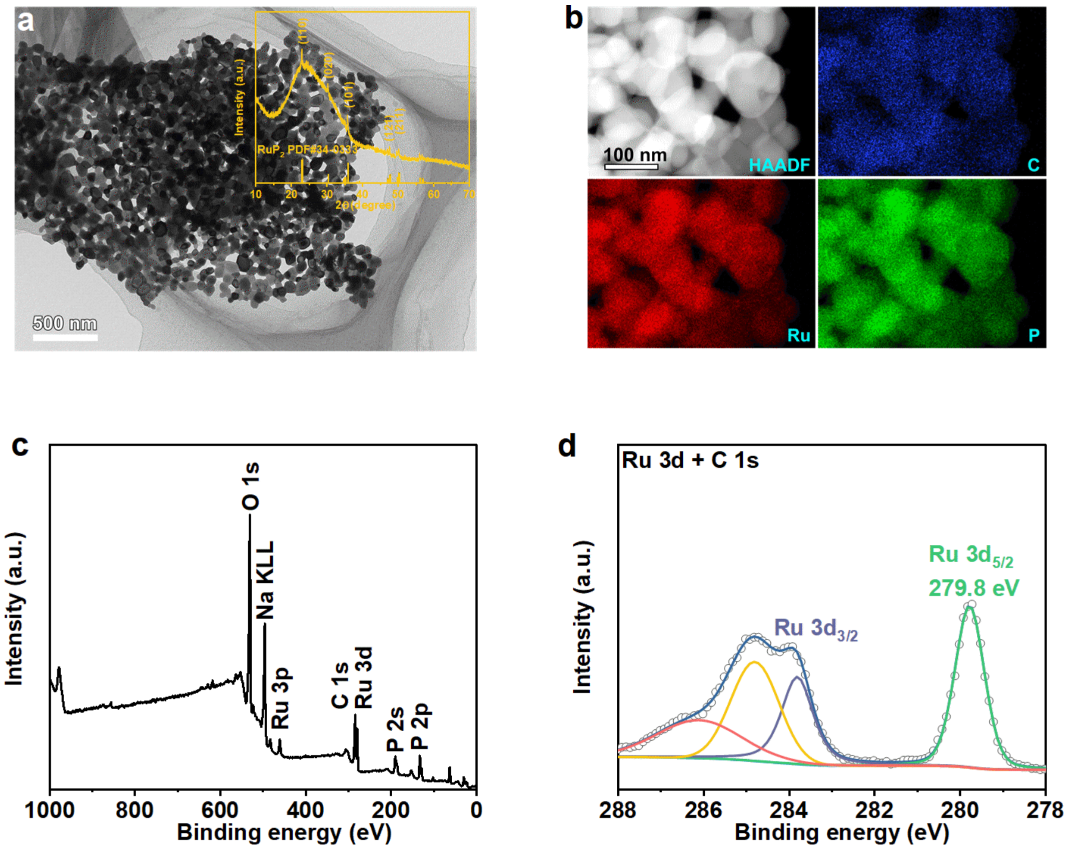

Figure S40. The stability investigation of RuP2@InC-MS after HER process in 1.0 M PBS: (a) The TEM image, inset shows the XRD pattern. (b) The HAADF-STEM and the corresponding EDS mapping. (c) The survey spectrum and (d) Ru 3d + C 1s high-resolution XPS spectrum.

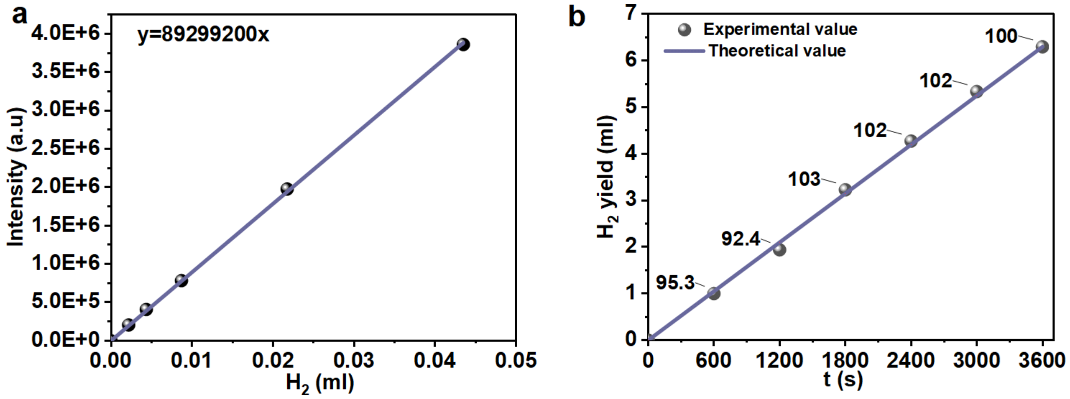

Figure S41. Investigation of the generated hydrogen amount in three-electrode configuration. The standard curve of hydrogen, (b) the theoretically calculated and experimentally measured hydrogen.

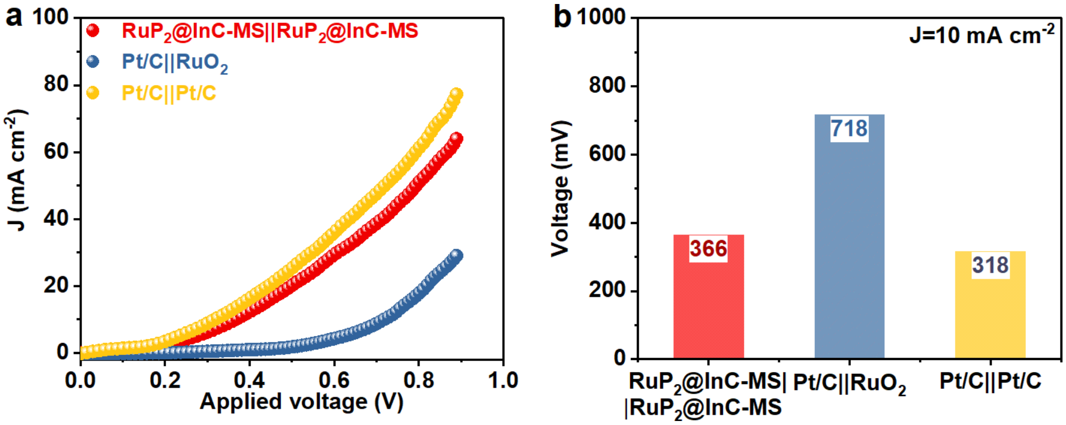

Figure S42. The comparation of OHzS performance. The comparing polarization curves of RuP$_2$@InC-MS||RuP$_2$@InC-MS, Pt/C||Pt/C and Pt/C||RuO$_2$ couples with a scan rate of 5 mV s^{-1} and (b) their corresponding cell voltages at 10 mA cm^{-2}.

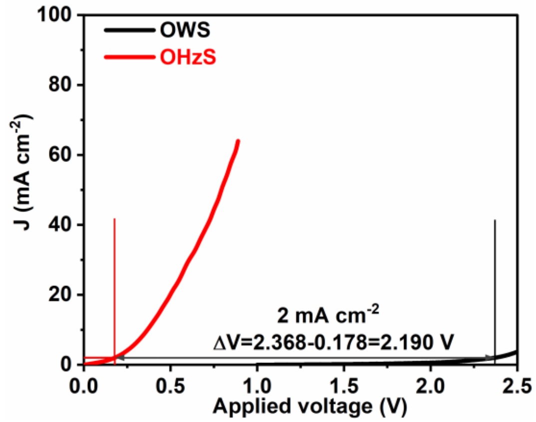

Figure S43. The LSV curves toward OWS and OHzS using RuP$_2$@InC-MS as bifunctional electrocatalysts.

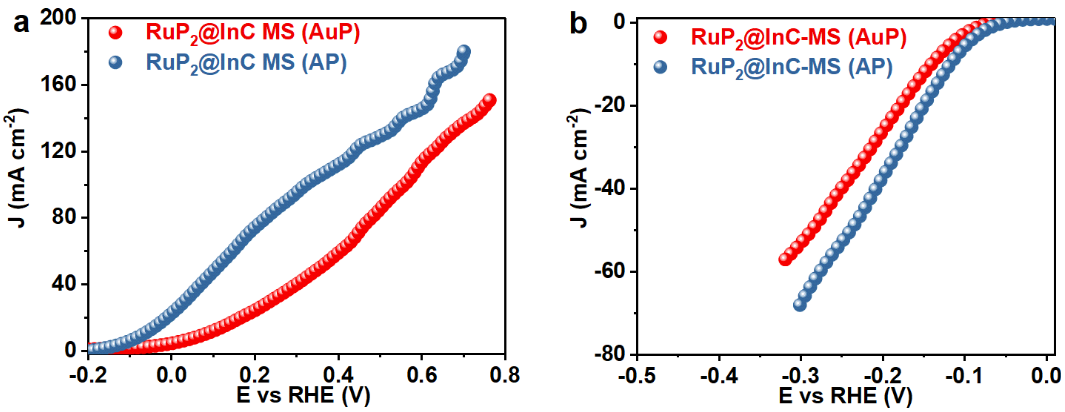

Figure S44. The HzOR (a) and HER (b) performance of RuP$_2$@InC-MS synthesized with different P sources.

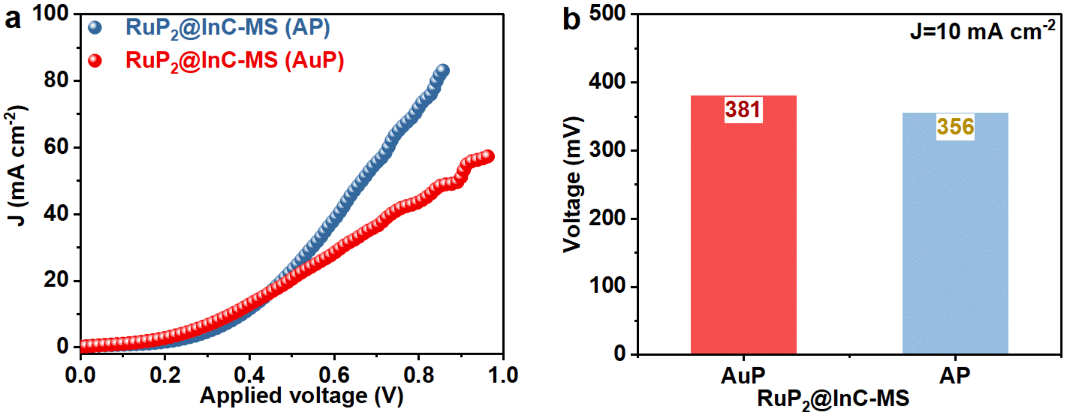

Figure S45. OHzS performance of RuP$_2$@InC-MS synthesized with different P source: (a) The LSV curves. (b) The applied voltages at 10 mA cm^{-2}.

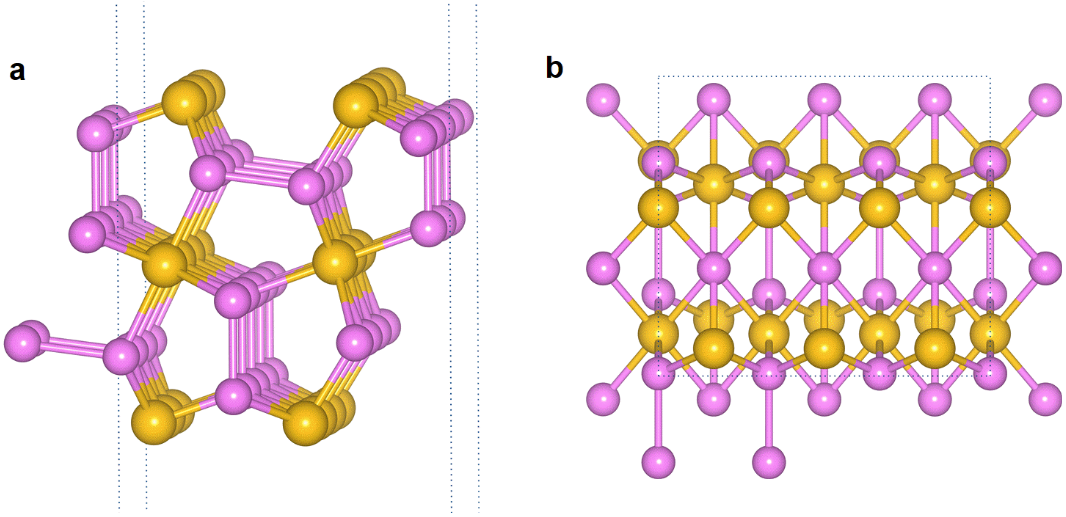

Figure S46. The DFT-relaxed structure model of RuP_2: (a) Side-view. (b) Top-view.

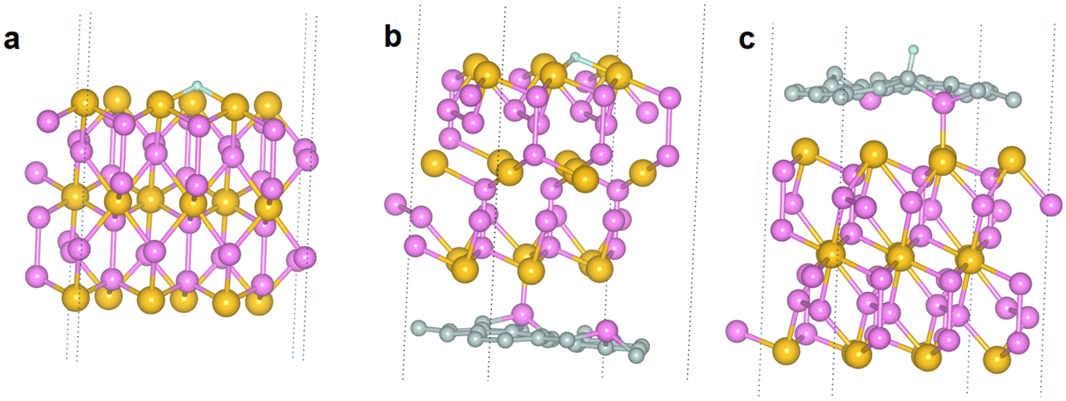

Figure S47. The H adsorption model: (a) Ru site in RuP_2. (b) Ru site in RuP_2@InC-MS. (c) C site in RuP_2@InC-MS.

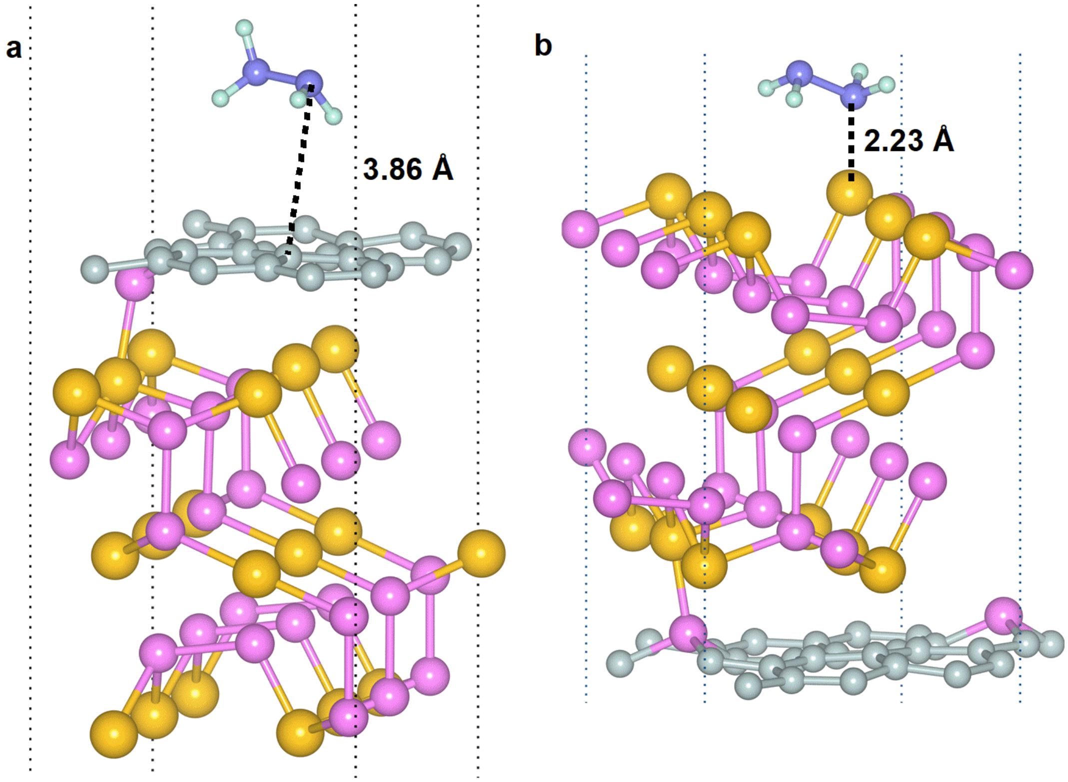

Figure S48. N_2H_4 adsorption on different sites of RuP_2@InC-MS: (a) Adsorption on the Ru site. (b) Adsorption on the C site. Numbers mean the bond distance between N atom in the N_2H_4 molecule and the nearest active atom in the RuP_2@InC-MS.

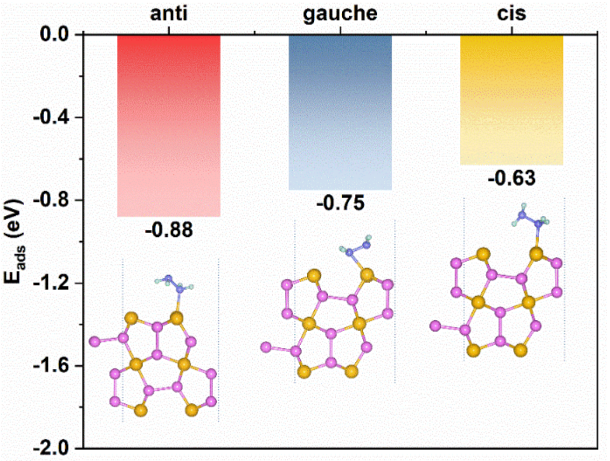

Figure S49. Different adsorption conformations of the N_2H_4 molecule adsorbed on the RuP_2 surface.

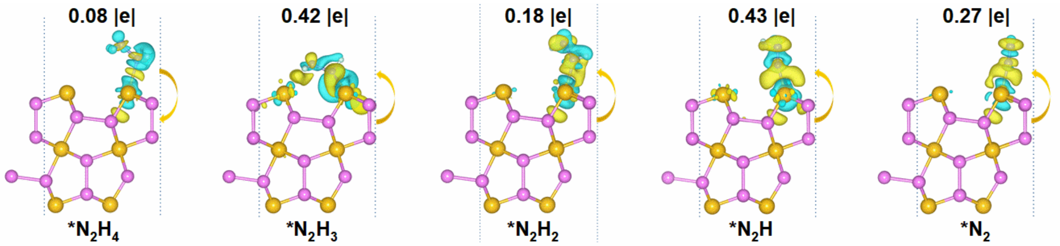

Figure S50. The Bader charge and charge density difference analysis for N_2H_4 dehydrogenation intermediates adsorbed on RuP_2 surface**.** The cyan and yellow region with the isosurface value of 0.005 $eÅ^{-3}$ represent charge depletion and accumulation, respectively. The arrow represents the direction of electron transfer and the values are the amount of Bader charge transferred.

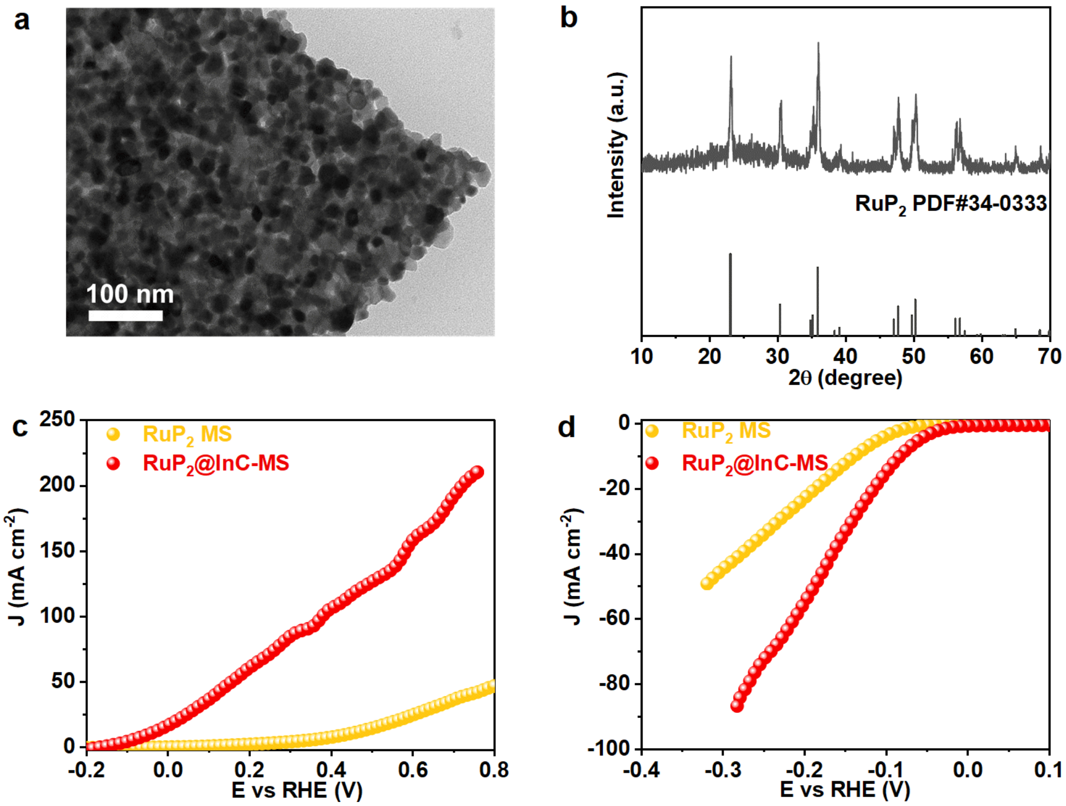

Figure S51. The morphology, phase and electrochemical performance of RuP_2 MS: The SEM image (a) and XRD pattern (b) of RuP_2 MS. (c) The comparing HER activity of RuP_2 MS and RuP_2@InC-MS in 1.0 M PBS. (d) The comparing HzOR activity of RuP_2 MS and RuP_2@InC-MS in 1.0 M PBS + 1.0 M N_2H_4.

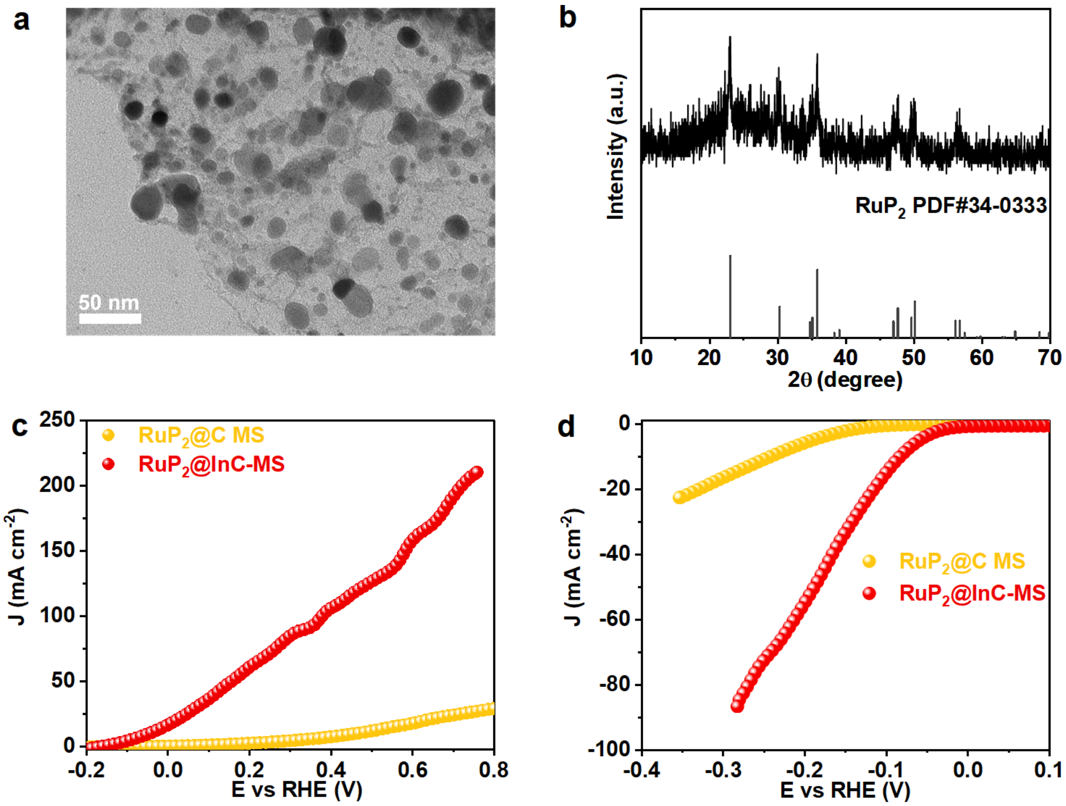

Figure S52. The morphology, phase and electrochemical performance of RuP_2@C MS: The SEM image (a) and XRD pattern (b) of RuP_2@C MS. (c) The comparing HER activity of RuP_2@C MS and RuP_2@InC-MS in 1.0 M PBS. (d) The comparing HzOR activity of RuP_2@C MS and RuP_2@InC-MS in 1.0 M PBS + 1.0 M N_2H_4.

3. Reference

1. G. Kresse and D. Joubert, Phys. Rev. B, 1999, 59, 1758-1775.
2. J. P. Perdew, K. Burke and M. Ernzerhof, Phys. Rev. Lett., 1996, 77, 3865-3868.
3. K. Reuter and M. Scheffler, Phys. Rev. B, 2001, 65, 035406.
4. H. Zhuang, A. J. Tkalych and E. A. Carter, J. Phys. Chem. C, 2016, 120, 23698-23706.
5. J. Zhang, F. Ren, M. Deng and Y. Wang, Phys. Chem. Chem. Phys., 2015, 17, 10218-10226.
6. Z. Wang, S. M. Xu, Y. Xu, L. Tan, X. Wang, Y. Zhao, H. Duan and Y. F. Song, Chem Sci, 2019, 10, 378-384.
7. Computational Chemistry Comparison and Benchmark Database. http://cccbdb.nist.gov/.
8. M. Yu and D. R. Trinkle, J. Chem. Phys., 2011, 134, 064111.
9. W. Tang, E. Sanville and G. Henkelman, J. Phys.: Condens. Matter., 2009, 21, 084204.